Large Scale Solution Assembly of Quantum Dot−Gold Nanorod Architectures with Plasmon Enhanced Fluorescence

Dhriti Nepal, Lawrence F. Drummy, Sushmita Biswas, Kyoungweon Park, and Richard A. Vaia*

Materials and Manufacturing Directorate, Air Force Research Laboratory, Wright-Patterson AFB, Ohio 45433-7702, United States

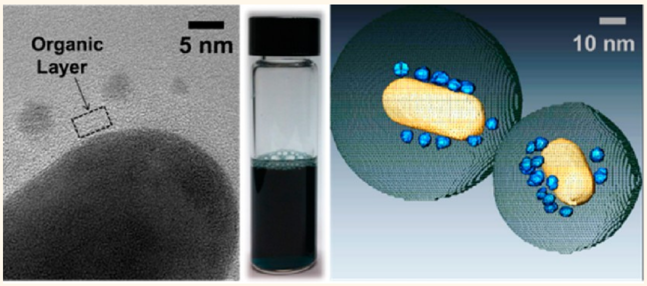

ABSTRACT Tailoring the efficiency of fluorescent emission *via* plasmon−exciton coupling requires structure control on a nanometer length scale using a high-yield fabrication route not achievable with current lithographic techniques. These systems can be fabricated using a bottom-up approach if problems of colloidal stability and low yield can be addressed. We report progress on this pathway with the assembly of quantum dots (emitter) on gold nanorods (plasmonic units) with precisely controlled spacing, quantum dot/nanorod ratio, and long-term colloidal stability, which enables the purification and encapsulation of the assembled architecture in a protective silica shell. Overall, such controllability with nanometer precision allows one to synthesize stable, complex architectures at large volume in a rational and controllable manner. The assembled architectures demonstrate photoluminescent enhancement (5×) useful for applications ranging from biological sensing to advanced optical communication.

KEYWORDS: gold nanorods · quantum dots · plasmon−exciton · controlled spacing · position · directed assembly · large-scale

Control of photon absorption and emission is at the core of many emerging photonic technologies,[1−3] ranging from SPASER,[2] photovoltaics,[3] and sensors[4] to single photon emitters for quantum encryption.[5,6] One approach to controlling the photophysics is chemical modification of the fluorophore (molecule or quantum dot) to adjust the energetics of its ground and excited states.[7,8] The creation of large fluorophore libraries is a synthetic challenge and limits tunability for many applications. An alternative approach is to modify the electromagnetic properties of the fluorophore by controlling its dielectric environment (*e.g.*, Purcell effect).[9] This approach is becoming increasingly popular as methods to precisely control the relative position and orientation of active optical units at the nanoscale have become available.[10,11] Interfaces,[12] microcavities,[13] nanorods,[14−18] nanospheres,[19−25] gratings,[26] and photonic crystals[27] have been used to engineer the radiative emission rate and quantum efficiency of fluorophores. Of these, fluorophore-metallic nanostructures are especially interesting because of the coupling of free space photons to collective oscillations of conductive electrons. This plasmon−exciton coupling offers a variety of opportunities for tailoring the fluorophore emission, including emission enhancement,[28] quenching,[28] directed emission,[6] or modulation of the emission spectral profile[16,18,29] *via* the right choice of materials, architectures, and excitation energy. This tunability is opening new avenues for single molecule detection and imaging in biological and medical sciences,[4,30] as well as solar energy harvesting and photonic plasmonic devices.[2,31]

Plasmons increase the spontaneous radiative emission by modifying the density of electromagnetic states in the emitter environment (weakly coupled regime) or by forming an plasmon−exciton state (strongly coupled regime). In the weakly coupled regime (first demonstrated by Drexhage *et al.*),[32] the emission rate of the dipole field can be estimated with Fermi's

* Address correspondence to richard.vaia@us.af.mil.

Received for review July 17, 2013 and accepted September 4, 2013.

10.1021/nn403671q

golden rule[33] and relates to the distance between the emitter and the metallic surface.[34] When the emitter is in close proximity (<10 nm) to the metallic structure though, overlap of energy states and collinear alignment of transition dipole moments results in strong coupling between the excited state of the absorber and surface plasmon modes. Nonradiative and radiative decay rates inversely depend on absorber–plasmon separation, so the optimum architecture in the strongly coupled regime depends on the spacing, location and orientation of the two species, as well as their emission and absorption wavelengths, resonance and nonresonance excitation, lifetimes and quantum yields.[28,31,35,36] Experimental reports on these variables are inconsistent and range from fluorescent enhancement[16,19,21,22,30,37−42] to quenching.[14,15,17,20,21,24,25,42,43]

For instance, Peng *et al.*[21] recently reported a systematic study showing that maximum enhancement and strongest quenching occurred at gaps of 21.9 and 2.8 nm, respectively, for spherical Au nanoparticle core surrounded by a shell of molecular dye, while Kulakovich *et al.* observed maximum enhancement with an 11 nm gap between CdSe QD and a AuNP colloidal film.[22] Large nonspherical plasmonic particles, including rods, triangles, and discrete clusters, are of current interest due to their larger scattering cross-section and spatial focus of the near field of the localized SPR (LSPR).[14,35,41,44] Fabrication of such noncentrosymmetric structures in solution remains a substantial challenge, where both photoluminescence enhancement[18,37,39−41] and quenching[15,17,18] have been reported.

One of the grand challenges in this emerging field is understanding structure–performance relationships in the strongly coupled regime with limited availability of well-defined structures with requisite spacing (<10 nm), position (relative orientation of dipoles), and interface (RMS roughness <0.2 nm). Since coupling depends very strongly on separation, control of the local structure beyond placing the plasmonic particle in a medium of emitters is crucial to optimize efficiency by deconvoluting the different phenomenon that dominate at small and large separation. Electron beam lithography provides routes to complex two-dimension structures,[6,45] but variability of gap size, surface roughness, and defect content are too high to systematically explore the strongly coupled regime. Colloidal approaches[46−49] have the promise to prepare precisely controlled three-dimensional structures with molecularly controllable gaps and geometries in scalable quantities if reproducibility and yield problems can be overcome. Solution assembly of spherical units *via* layer-by-layer deposition on particles,[22,42] direct chemical coupling using molecular/biological linkers,[19,20] or sequential silica encapsulation[14,38,40,43] have shown impressive precision if the surface functionalization and colloidal stability throughout the assembly process can be optimized. Similar assembly with anisotropic nanoparticles, however, still remains a challenge, since location and orientation of the fluorophore in addition to gap size must be controlled while avoiding instability of the intermediates during the ligand exchange and assembly. Therefore additional methods are required to produce anisotropic emitter-plasmon nanostructures so as to forward the understanding of spacing, location, and dipole orientation on coupled plasmon–exciton photophysics.[11,35,36,44] One critical factor limiting the high-yield low-variability assembly is systematic control of the various crystal facets of the initial nanoparticle, such as a gold nanorod (AuNR). While there has been substantial progress over the past decade in developing recipes for different size and shape AuNRs,[50,51] only recently has the underlying mechanism of growth been sufficiently understood to provide sufficient control of AuNR shape and surface structure to enable selection of facet reactivity for subsequent assembly.[48,52]

Here we report a simple, facile, general process that addresses many synthetic challenges to provide controlled organization of quantum dots (QD) on AuNRs. Control of the position, spacing and quantity of QDs per AuNR is achieved through anisotropic surface functionalization of the AuNR with organic molecules of increasing size. The number of QDs per AuNR was controlled by the extent of initial ligand exchange of the AuNR and the QD concentration. This process provides QD-AuNR nanostructures that are stable in aqueous solution and that can be encapsulated with silica. This allows for the isolation of QD-AuNR nanostructures and the high-resolution characterization of their 3-dimensional structures and evaluation of the photophysics in solution and on surfaces.

RESULTS AND DISCUSSION

Figure 1 summarizes the general process for assembly of QDs and surfactant stabilized AuNR. Specific procedures are detailed in the Methods section below. The most critical characteristics are (1) the concentration of a stable suspension of purified AuNR where excess surfactant stabilizer has been reduced; (2) the use of a single solvent system for assembly, ligand exchange, surface functionalization, functional group conversion, and particle coupling; and (3) controlling the rate and order of reactant addition at each step. These factors reflect that particle assembly is a kinetic process where we are not only trying to drive uniformity from random collisions between particles, but also striving to control the evolving characteristics of particles, their surfaces, and reactant intermediates.[49] We have found that successful dispersion of individual reactants (particles, ligands, etc.) is paramount to ensuring the uniformity of particle–particle coupling and ligand exchange, while sedimentation or other processes to concentrate particles lead to unwanted

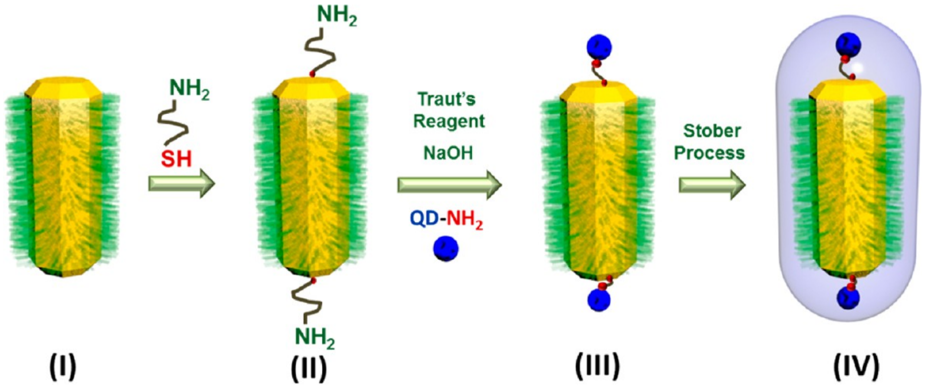

Figure 1. Schematic of directed assembly of QD-AuNR architectures in water. CTAB stabilized AuNR (I) was preferentially functionalized at the end with thiolated amine (II). Traut's reagent was used to convert the terminal amines of the QD and AuNR to drive assembly by dithiol coupling (III). The resulting aqueously stable structure was encapsulated in silica *via* the Stober process (IV). The schematics are not to scale.

particle–particle interactions and undispersible aggregates. Surface functionality is controlled by ligand exchange and depends on time as well as the relative concentration of surface modifiers and molar concentration of nanoparticles.[53] In addition, AuNR crystal facet chemistry evolves on a time scale of hours to days,[52] so the reaction medium and feed rates of reactants, ligands, and particles can have substantial impact on the yield and structure of the final product.

In a typical synthesis, single-crystalline AuNRs were made using the seed mediated growth process with a 5 min seed aging time.[48,49,52] On the basis of the AuNR growth mechanism,[52] this provides optimal control for ligand exchange. Water in contrast to organic solvents was chosen as the assembly medium since it affords two long-range stabilization motifs (electrostatic and steric), in addition to eliminating the need for particle transfer. After removal of spherical nanoparticle impurities and excess CTAB as outlined previously,[48] the purified AuNRs **(I)** (length = 50 ± 5 nm, width = 20 ± 5 nm) was used within 72 h for partial ligand exchange of CTAB with aminoalkylthiols, such as 11-Amino-1-undecanethiol hydrochloride (AUT). Here the amino functional alkythiol was chosen over other bifunctional ligands because of its good aqueous solubility and negligible effect on AuNR dispersion due to its compatibility with CTAB. Additionally, the amino terminus provides a platform for a diverse array of simple and efficient chemical reactions (*e.g.*, nucleophilic addition and substitution) in aqueous solution. Finally, Au-amine bonding is weaker than Au-thiol,[54] leading to preferential orientation of the amine away from the surface.

Site specificity of the ligand exchange is achieved by using freshly prepared AuNRs and adjusting CTAB concentration (**II**). CTAB forms a robust bilayer on the AuNR surface, and its stability is influenced not only by AuNR facet and local curvature, but also by concentration of CTAB and solution temperature.[52] For example, CTAB forms a robust bilayer on the {2 5 0} side facets of the rod, whereas the pyramidal end facets, which consist of {3 0 1} and {3 1 0} planes, are believed to frustrate CTAB absorption and packing,[52] resulting in a less stable bilayer at the rod ends. CTAB therefore preferentially desorbs from the ends *versus* the sides as CTAB concentration is decreased toward its critical micelle concentration. Likewise, cosurfactants or other ligands are preferentially absorbed within this weaker, less dense bilayer relative to the more stable sides. As a result, the added alkylthiols initially prefer the AuNR ends, resulting in an end-functionalized rod with an intact cationic stabilization on the sides.[49] Thus, by controlling CTAB concentration and reaction time (Supporting Information, **S I**), AUT functionalization can be achieved primarily at the AuNR ends (**II**) or all around the surface. For example, AuNRs with AUT preferentially at the ends were achieved at 0.03 M CTAB and short ligand exchange time (30 min). In contrast, lower CTAB concentration (0.005 M) and longer reaction time (>1 h) resulted in uniform AUT functionality across the AuNR surface. To tune QD-AuNR spacing, ligand exchange was performed with different length aminoalkylthiols [6-amino-1-hexanethiol hydrochloride (AHT), 3-amino-1-propanethiol hydrochloride (APT)]. As the length of alkyl chain decreases, the steric hindrance of the chain decreases. As a result, stability of AuNR in the aqueous solution became very sensitive to CTAB concentration and reaction time. Thus, the AHT and APT reaction were conducted with higher CTAB concentration and lower reaction time. UV–vis spectra shows that the AuNRs remain well dispersed throughout the processes (Supporting Information, Figure S1).

As noted above, amino functionality provides a flexible platform for subsequent conjugation in water. Particle–particle coupling can follow one of two strategies: (1) direct binding between two complementary surfaces (A–B); or (2) coupled binding of nonreactive surfaces by a complementary linker (A–B–B–A). Conceptually, coupled binding provides more control due to the ability to separate particle bonding from the particle stability motif (steric and electrostatic), as demonstrated using DNA functionalized nanoparticles and linkers.[55] We follow a variant of these strategies beginning with nonreactive surfaces, and selectively couple the linker to one particle before inducing particle–particle coupling by controlling the relative feed ratios and molar concentration of the two particles. Specifically, the terminal amines on polyethylene glycol (PEG) stabilized QD (e-bioscience)[56] are converted to thiols through an excess of Traut's reagent (2-iminothiolane HCl). Traut's reagent provides a simple, highly efficient aqueous approach to link amines through a disulfide bridge that is "orthogonal" to the residual cationic stabilization of the AuNRs. The QD to AuNR ratio is then simply controlled by the slow addition of predetermined amount of QD–Traut solution to the AuNR solution (**II**) ([QD]/[AuNR] ~ 0.1–12.5). Excess Traut's reagent present in the QD solution is sufficient to spontaneously convert amine to thiol on the AuNR surface and afford disulfide bond formation *via* oxidation of sulfhydryl groups between QD and AuNR, resulting in the assembly QD_n/AuNR (**III**) nanostructures, where *n* refers to number of QD attached on a single AuNR. The formation of the assembly is confirmed by dynamic light scattering, which shows an increase in hydrodynamic size (Supporting Information, Figure S2). We note that direct AuNR coupling ({AuNR}–S–S–{AuNR}) was rarely observed under these reaction conditions. This is most likely due to several factors, including strong electrostatic stabilization of the cationic, CTAB-stabilized AuNRs, steric factors (slower translational diffusivity of bulky AuNR relative to substantially smaller QDs), low number density of AuNRs (<1 nM), and relatively low molar concentration of the Traut's reagent (1 mM). For example, if surface amines of the QD and AuNR are initially converted into thiols, substantial aggregation occurs upon mixing, especially self-aggregation of the AuNR.

The QD-AuNR nanostructures are stable in water, providing for storage, processing or additional chemical functionalization, including encapsulation with silica *via* the Stober process (**IV**). The stability and low reactivity of these encapsulated nanostructures allows for broader applications[57] in aggressive environments such as high temperature,[49] or intense laser irradiation.[58] In addition, the order of particle addition results in a very small amount of unbound (free) QD: less than 2% for optimized conditions. This assembly efficiency negates subsequent purification to remove unbound QD. We note that the colloidal stability depends on the length of the linker and the extent of QD coupling. For example, solutions of AuNRs with AUT end-linked QDs are stable in water for more than 2 weeks, while AuNRs fully surrounded by AUT linked QDs begin to settle in less than 2 days. This is likely due to the inability of the short PEG grafts on the QDs to provide sufficient steric stabilization to counter the reduced electrostatic stabilization resulting from less CTAB.

By employing these methodologies, Figure 2 demonstrates the ability to control the spacing, location and relative number of QD surrounding the AuNR by changing the length of the alkylthiol ligand [AUT (11 alkyl chain) and AHT (6 alkyl chain)] . Figure 2a–j qualitatively shows that the longer AUT (end-to-end size ~1.6 nm) provides a larger spacing than AHT (end-to-end size ~0.9 nm). Accurate, quantitative measurements of the gap need to take into account the factors that can affect sample preparation, including dehydration of the organic spacer, electron beam damage, drying effects on the QD arrangement, and the two-dimensional nature of microscopy projections of the three-dimensional distribution of QD around the AuNR. This is illustrated in Figure 3, which compares bright field, scanning TEM (STEM), and 3D tomographic reconstruction of QD_n/AuNR. The two-dimensional projection does not reveal QDs bound to the top (and bottom) of the rod with a long axis in the image plane. Electron tomography of bare QD_n/AuNR (Supporting Information, Figure S12) showed preferential arrangement of the QDs against the TEM grid, reflecting drying distortion and leading to abnormally large QD-AuNR spacings. In contrast, electron tomography of silica encapsulated assembles (discussed below) shows that the spacing between the AuNR and QD are 2.5 ± 1.0 nm and 1.8 ± 0.2 nm for AUT and AHT, respectively. The extinction spectra of solutions of encapsulated and unencapsulated assemblies (Supporting Information, Figure S10) were identical when the predicted 50 nm shift of the longitudinal LSPR due to the change in local refractive index is taken into account.[59] This demonstrates that silica encapsulation does not substantially disrupt the local structure of the QD-AuNR assembly. Taken together these data show that the uniform organic separation distance is due to the difference in chain length for AUT (11 alkyl chain) and AHT (6 alkyl chain).

The selective attachment of the QD to the AuNR ends can be achieved by using short time amino functionalization of AuNR suspensions with low CTAB concentration. Figure 2a,f shows QD at AuNR ends with spacer AUT and AHT, respectively, for assemblies prepared using equimolar concentrations of QD and AuNR. In a typical reaction with 0.2 nM QD added to a 0.2 nM solution of AUT functionalized AuNR product, we found a yield of AuNR bound with QD of 75%. Figure 2k shows a typical distribution (blue dots, the line for clarity only) of QD_n/AuNR from the product after analyzing >750 structures from TEM (Supporting Information, Figure S4). Among the assembled products we found 70% were QD_1/AuNR, ~20% were QD_2/AuNR, and the remaining structures were QD_{3-4}/AuNR. Figure 2b and 2g are typical examples of QD_2/AuNR with the spacer of AUT and AHT, respectively.

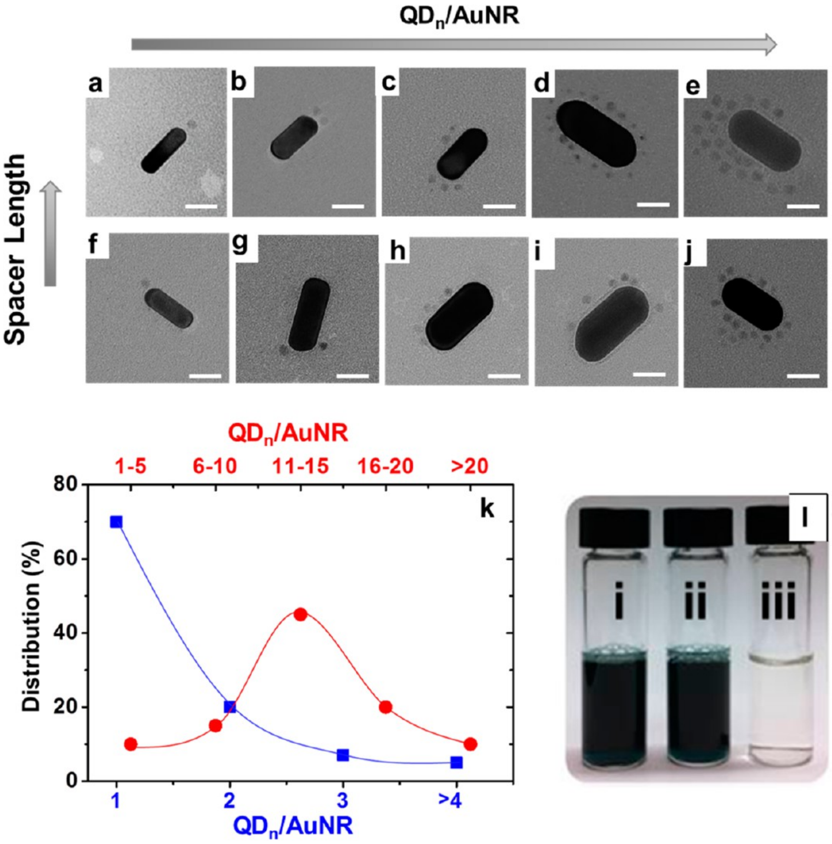

Figure 2. Structural control of QD-AuNR assembly in aqueous solution. TEM images (scale bar = 25 nm) showing control of spacing, position and QD_n/AuNR (n is the number of QD per AuNR). Spacing length is controlled by changing ligand length [AUT (a−e), AHT (f−j)]. Ligand position and QD_n/AuNR is controlled by incrementing QD concentration from 0.2 (a,b,f,g), 0.5 (c,h), 1.5 (d,i), 2.5 nM (e,j) at 0.2 nM AuNR concentration. (k) Distribution of QD_n/AuNR in the reaction solution with 0.2 nM QD (blue) and 2.5 nM QD (red) (the lines for clarity only). (l) Picture of vials containing aqueous solutions of (i) AuNR (0.7 nM), (ii) QD_n/AuNR (product from 0.7 nM AuNR and 1.4 nM QD), and (iii) QD (1.4 nM).

Control over the number of QD surrounding the AuNR, QD_n/AuNR is achieved by increasing the stoichiometric ratio of amino functionalized QD to AuNR (**III**) to provide more anchoring sites by increasing the fraction of aminoalkylthiol ligand exchange on the AuNR. For example Figure 2c−e and 2h−j show product from 0.2 nM AuNRs modified by ligand exchange with AUT and AHT, respectively, and QD solutions with increasing concentrations (0.5, 1.5, and 2.5 nM) (more images in Supporting Information, Figures S5−S8). These experiments show that increasing QD concentration directly influences the QD-AuNR architectures. Figure 2c and 2h are the typical products obtained from 0.5 nM QD concentration for spacer AUT and AHT, respectively. At 1.5 nM, the AuNR is completely surrounded by the QD (Figure 2d,i). At 2.5 nM, the QD concentration is sufficiently in excess that a double layer (Figure 2e and 2j) forms, most likely because of sulfydryl coupling between QDs. As expected, the distribution of structure types is broader for the higher QD concentration. For example, the distribution of QD_n/AuNR in the product from 2.5 nM QD and AUT AuNR are shown in Figure 2k (red dots, the line for clarity only). Here ∼15% of the product were $QD_{<10}$/AuNR, ∼65% were QD_{10-20}/AuNR, and ∼10% were $QD_{>20}$/AuNR. This distribution can be improved through optimization of assembly conditions (time, temperature, concentration, feed ratio, and stirring) and uniformity of partially ligand-exchanged AuNR (surface facet, shape, and size). Overall, these results emphasize the necessity to understand, and balance the various exchange rates (ligands and surface reconstructions), collision rates (particle size and concentration), and chemical kinetics (linker binding), to control the assembly (Figure 1). Despite this apparent complexity, the overall yield of the QD assembled AuNR product even at high QD to AuNR ratios is close to 98%; that is, only ∼2% of the QDs are not attached to AuNRs. This is significantly important in terms of the materials purity in a stable aqueous solution since removing such a tiny unreacted QD using a common purification process is not straightforward.[60] An additional benefit of our method (Figure 1) is that it can be easily scaled up to fabricate products at the gram scale in solution. A picture of a vial containing 5 mL of aqueous solution of QD_n/AuNR nanostructures (product from 0.7 nM AuNR and 1.4 nM QD) is shown in Figure 2l. The product color (ii) (dark green) is similar to that of the

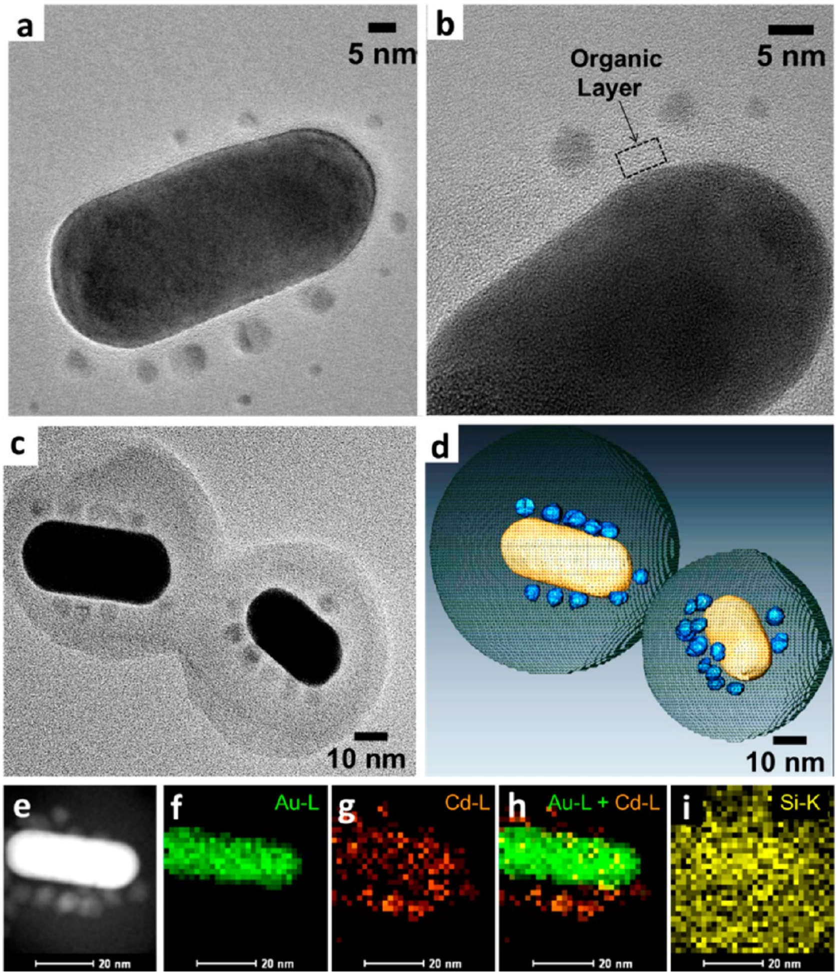

Figure 3. Morphological characterization of QD_n/AuNR architecture by high resolution TEM before and after silica encapsulation. (a) A bright field image of a typical individual QD_n/AuNR architecture showing overall morphology and (b) selected area magnified image of the architecture showing the organic space between AuNR and QD. (c) A typical silica encapsulated QD_n/AuNR architecture using HR-TEM (Bright Field), and (d) its corresponding reconstructed image from MBIR, showing three-dimensional arrangement of the QDs around the AuNR. (e−i) Elemental mapping from STEM image of silica coated QD-AuNR architecture (e) (scale bar for all images = 20 nm), and its corresponding mapping images of (f) Au (L_α 1.01 keV), (g) Cd (L_β 3.53 keV), (h) Au (L_α) + Cd (L_β), and (i) Si (K_β 1.83 keV).

pristine AuNR (i), while quantum dots at an equivalent concentration is colorless (iii). The nanostructures are highly stable with no visible precipitation of QD_n/AuNR for more than two weeks at room temperature.

Figure 3 shows additional analytical characterization of the bare and silica encapsulated QD_n/AuNR assemblies *via* AUT spacer. High magnification bright field TEM images (Figure 3a and 3b) show a high resolution view of the assembly. Lattice fringes of both the AuNRs and QDs are more visible in expanded images (Supporting Information, Figure S9), and in some instances, the core−shell structure of the CdSe/ZnS (darker/lighter) QD can also be observed. The images consistently show amorphous material in the gap between the AuNR and QD (Figure 3b), consistent with the organic spacer being a combination of alkylthiol, residual CTAB and the aminated PEG[56] stabilization shell surrounding the QD. Figure 3c shows a typical silica encapsulated QD_n/AuNR nanostructures for comparison. Because of the excellent aqueous stability of the QD-AuNR assembly, the Stober process simply encapsulates the entire assembly, resulting in a silica particle with a single AuNR core that is surrounded by individual QD (additional images in Supporting Information, Figure S10). High angle annular dark field-scanning transmission electron microscopy (HAADF-STEM) tomography improves the contrast between QD, silica and AuNR and allows for chemical mapping using X-ray energy dispersive spectroscopy (XEDS). This enables direct reconstruction of the internal structure of the assembly and hybrid particle and allows for the detailed analysis of the 3D morphology at sub-nanometer resolution.[61] The model based iterative reconstruction (MBIR) technique is used to reconstruct (HAADF-STEM) tomography data,[62] and Figure 3d is a snapshot of a 3D rendering of the tomographic reconstruction of a same region. The reconstructed image is portrayed at slightly tilted angle compare to the

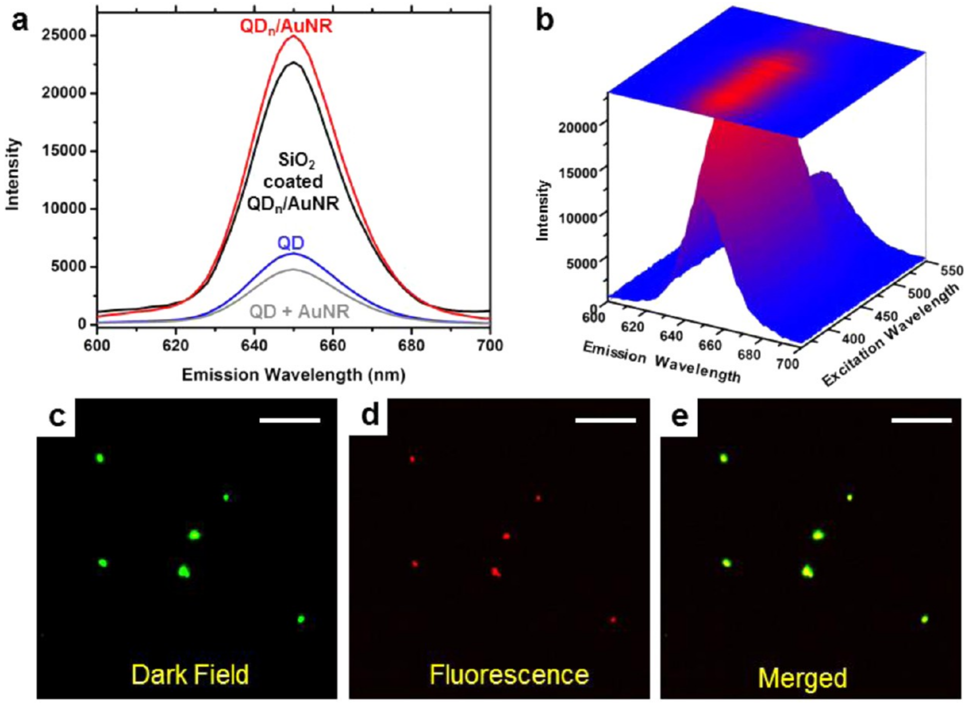

Figure 4. Photophysical properties of QD$_n$/AuNR in aqueous solution and on glass surface. (a) Photoluminescence spectra of aqueous solutions of equimolar QD concentration (0.4 nM): QD$_n$/AuNR ($n = 3 \pm 1$, in which >50% of QD are at AuNR ends) (Red); its silica encapsulated product (Black); base mixture of QD (0.4 nM) and AuNR (0.2 nM) in the absence of AUT spacer (Gray); and control QD (absence of AuNR) (Blue). (b) A combination of 2D and 3D counter plot of PL spectra of QD$_n$/AuNR acquired at different excitation wavelength from aqueous solution showing an emission maximum at 650 nm. Bottom images are obtained from dark field hyperspectral imaging microscope using dual imaging modalities of QD$_n$/AuNR architectures spread between two glass coverslips. (c) Dark field scattering (570 nm excitation). (d) Fluorescence emission (570 nm excitation; fluorescence collected at 610 nm with long pass filter). (e) Merged image of (c) and (d) showing overlap of signals confirming the sample purity. The scale bars are 10 μm.

reference to visualize the distinct gap as well as the organization of QD on the AuNR surface. The corresponding STEM, snapshots of different tilt angles of reconstructed images (Supporting Information, Figures S11−S13), and its video are in the Supporting Information. STEM-derived elemental mapping of the silica encapsulated structure in Figure 3e is shown in Figures 3f−i, which shows clear correlation of composition to structure: (f) Au (L_α 1.01 keV), (g) Cd (L_β 3.53 keV), (h) Au (L_α) + Cd (L_β), and (i) Si (K_β 1.83 keV). Other elements present in the structure such as zinc and sulfur were also clearly mapped (Supporting Information, Figure S14).

The availability of milliliters of solution from the large-scale fabrication of QD$_n$/AuNR architectures (Figure 2l) permits macroscopic examination of ensemble-averaged photophysical processes, such as plasmon−exciton coupling. As an example of the emission characteristics of the assemblies, Figure 4a compares the photoluminescence (PL) spectra from various control solutions with equimolar concentration of QD (0.4 nM) relative to a QD$_n$/AuNR assembly with $n = 3 \pm 1$ and >50% of the QDs attached at the AuNR ends with AUT. This architecture was obtained by reacting 0.4 nM CdSe/ZnS QD (emission wavelength, 650 nm) with 0.2 nM of AuNR (LSPR peak ~650 nm). For excitation (470 nm) that is nonresonant to the LSPR (650 nm), the photoluminescence from bare and silica encapsulated QD$_n$/AuNR is approximately 5-times greater than from an equimolar QD solution. QD solution (0.4 nM) in the presence of unbound AuNR (0.2 nM) showed slightly less emission than the control QD solution, because of the large distribution of separation distance between QD and AuNR in the random mixture. This random mixture includes a fraction of particles with large separation, no emission enhancement, and lack of coupling, as well as a fraction of aggregated particles with no separation, which leads to emission quenching. These observations corroborate previous studies and emphasize the criticality of optimizing the distance between all the emitters and the plasmon surface.[15] Note that no significant change in photoluminescence spectrum of the QD$_n$/AuNR assembly was observed after silica encapsulation. This is also similar to some prior reports.[63] The extent of nonradiative process within a QD depends on the band gap of its local surrounding. None of the processes used during assembly will replace the robust organic shell (PEG derivative) that initially stabilizes the CdSe/ZnS QDs. Thus the "baseline" QD and assembled QDs have similar organic shells surrounding the outer ZnS shell (3.9 eV), which initially provides relatively good carrier confinement. The slightly reduced intensity of the silica encapsulated product relative to the nonencapsulated product is attributed to an estimated 10% uncertainty in concentration and composition of QD-AuNR architectures. This was evaluated on the basis of 3 independent reactions where concentration variation due to inherent limitations of solution measurement (pipetting) and minor variation in purity and concentration of the initial AuNRs was determined to be the major factors. Additionally, background scattering increased with silica shell growth, further challenging highly quantitative comparison of raw measurements.[63]

A complete excitation−emission mapping of the QD_n/AuNR is shown in Figure 4b. Here the emission spectrum was collected from 600 to 700 nm from a nonresonant excitation (350−550 nm) with respect to LSPR of the AuNR (650 nm). The 2D projection at the top of the graph shows the highest emission enhancement from 425 to 500 nm with no spectral modulation. This is consistent with prior reports on nonresonance excitation of other dipole-plasmon couples.[24,25] Note that in the case of excitation resonant with the LSPR, the spectral profiles have been shown to be modulated because of plasmonic emission.[18]

Figure 4c shows dark field hyper-spectral scattering images of a drop dried solution on glass using 570 nm excitation. Each green dot corresponds to scattering from AuNRs. Fluorescence from the same region (Figure 4d) (excitation at 570 nm, emission at 650 nm) confirms the presence of QDs, since AuNRs do not fluorescence under these conditions. The overlap of the two images (Figure 4e) corroborates the assembled architecture, and confirms the solution purity and shows that a very small fraction of unbound QDs are present. In general, we observe enhancements between 2.5 and 5 times, where the higher enhancements correspond to systems where extra care was used to remove small Au nanoparticle clusters and unreacted seeds (<5 nm). These small Au clusters are known to quench PL.[20] Overall, these enhancements, which are averaged over the ensemble, are greater than prior reports (1.5×) of comparable architectures (QD-AuNR with silica spacer)[40] and approach 65% of values estimated from theory for nonresonance excitation.[36] This QD_n/AuNR architecture demonstrates that the assembly approach provides sufficient control to observe PL enhancement from QD−plasmonic nanoparticle structures with sub 5 nm spacings. With this foundation to create and measure PL enhancement, future studies can provide experimental data with respect to spacing, orientation, and number of emitters to compliment current modeling and theory, which are taking into account the additional quantum and dipole−dipole couple effects that occur at these ultrasmall spacings.

CONCLUSION

In summary, we have demonstrated a flexible and facile solution methodology for fabricating large quantities of highly stable, defined QD_n/AuNR architectures using common organic compounds. Using covalent coupling in aqueous solution, a variety of QD_n/AuNR architectures was prepared with control of the relative location and nanoscale spacing that parallel prior reports using biomacromolecules. These factors can be independently tuned by the choice of molecular spacer, concentration, ligand exchange time, and the QD stoichiometric feed ratio. The technique enables large-scale fabrication due to the high yield of the QD-AuNR conjugation (98% QD bound to AuNR) and its long-term aqueous stability (days to weeks). The stability also affords substantial flexibility for further processing; including encapsulation of the complexes by silica to improve their environmental stability for applications with extreme environmental demands (*e.g.*, high temperature, large fluence and chemicals). Additionally, the encapsulation provides a route to overcome sample preparation artifacts and enable nanoscale quantification of the three-dimensional structure using high resolution TEM. Because of the precision in positioning the QD at the AuNR tip, PL was enhanced ∼5 times for a solution ensemble. This enhancement is approaching 65% of the value estimated from theory for nonresonant excitation.[36]

Overall, these simple and highly efficient techniques are illustrative of emerging routes for bottom-up colloidal concepts to challenge traditional lithographic approaches for fabricating plasmon-enhanced photonics. Substantial challenges though still remain to further narrow the distribution of spacing, composition (location, QD/AuNR ratio) and three-dimensional structure. We believe this refinement will be possible with additional understanding of a few factors. Improved insight on the relation between the local structure and composition of the surface stabilization layers and crystal facets of the nanounits will enable more precise site-specific ligand exchange. The underlying Brownian dynamics, entropic factors, and randomness of particle−particle collisions will ultimately limit the structural variability of the assembled architectures though, and thus postassembly refinement techniques will most likely be required. Purification techniques in the mode of those used in organic chemistry, as shown herein, will also be required to meet the established standards for lithographic-derived devices. Finally, refined plasmon−exciton design criteria will require direct quantitative comparisons between theory, ensemble, and single particle performance. For example, higher Purcell Factor and further enhanced emission of QD_n/AuNR assemblies are excepted with additional system optimization,[34,43] including the use of AuNRs with higher scattering cross-section (*i.e.*, larger AuNR volume), QDs with emission on the low energy side of the LSPR (*i.e.*, Stokes shift increases apparent quantum yield) and excitation resonant to the LSPR to increase radiative decay. Alternatively, such design optimization would also enable modulation of the emission profile[16,18,29] or emission that can be steered using polarized light.[28] In general, the single phase solution assembly with low cost ligands provides a framework to achieve the request design flexibility. As such, large-scale and high yield assembly of well-defined QD_n/AuNR architectures in aqueous solution opens up new possibilities for practical applications including displays, solar cells, sensors, single photon sources, biomedical devices, and advanced optical communication devices.

METHODS

Materials. Hexadecyltrimethylammonium bromide (CTAB) (98%), benzyldimethylhexadecylammonium chloride hydrate (BDAC) (98%), and L-ascorbic acid were purchased from Tokyo Chemical Industry. Chloroauric acid ($HAuCl_4$) (99.999%) and sodium borohydride ($NaBH_4$) (>95%), 11-amino-1-undecanethiol hydrochloride (AUT) (99%), 6-amino-1-hexanethiol hydrochloride (AHT), 3-amino-1-propanethiol hydrochloride (APT), (3-mercaptopropyl) triethoxysilane (MPTES) (>80%), and sodium hydroxide (NaOH) (>98%) were purchased from Sigma-Aldrich. Silver nitrate ($AgNO_3$) (electrophoresis grade) was purchased from ACROS. All chemicals were used as received without further purification. Deionized water (18.2 MΩ), obtained from Milli-Q water purification system was used in all the experiments. Amine functionalized core–shell CdSe/ZnS quantum dots ($\lambda_{emission}$ = 650 nm) in aqueous solution were purchased from eBioscience, Inc., San Diego, CA, and used as received. Traut's reagent (2-iminothiolane HCl) was obtained from Thermo Scientific and used as received. Glass slides (Sigma-Aldrich) and immersion oil (CytoViva Inc.) were also used as received.

Gold Nanorod Synthesis. AuNRs were synthesized by the seed-mediated growth process in CTAB solutions in the presence of $AgNO_3$, as reported previously.[64,65,52] To ensure reproducibility of the subsequent steps, we set the temperature at 25 °C for all reactions. The growth solution was prepared by mixing $HAuCl_4$ (0.5 mL, 0.1 M), $AgNO_3$ (0.08 mL, 0.1 M), and CTAB (100 mL, 0.1 M) followed by addition of the ascorbic acid solution (0.55 mL, 0.1 M) as a mild reducing agent. The seed solution was prepared by dissolving $HAuCl_4$ (0.025 mL, 0.1 M) in an aqueous solution of CTAB (10 mL, 0.1 M). The bright yellow transparent solution was stirred for 1 h. A freshly prepared, ice-cold $NaBH_4$ solution (0.6 mL, 0.01 M) was then added into the mixture under vigorous stirring. After 5 min, 0.1 mL of this seed solution was added into the previously prepared growth solution and shaken for 5 min. The color of the reaction solution slowly changed from clear to violet and finally green (for aspect ratio 2.5), indicating the growth of AuNR. The as-made AuNR solution (or the solution of interest) was kept in an Erlenmeyer flask at 25 °C for 15 h. The solution was then centrifuged at 7500 rpm for 1 h, and the brownish-green residue (from bottom) (in ~10% of supernatant) was carefully collected, leaving behind a pink residue on the tube sidewalls. The green solution (with some supernatant) from the collected residue was centrifuged again at 10 000 rpm for 10 min. The supernatant was carefully discarded, and the bottom residue was slowly dissolved in 0.1 M CTAB solution, vortexed for 1 min, and kept at room temperature for 1 h. We found that this 1 h storage helped to restore CTAB bilayer on AuNR surface, otherwise repeated centrifugation leads to AuNR precipitation. The same process was repeated three times to ensure the removal of small unreacted gold seed (<3 nm) from the supernatant. Concentrations of the AuNR were calculated using $\varepsilon = 1.425 \times 10^9$ M^{-1} cm^{-1}, $\varepsilon = 1.326 \times 10^9$ M^{-1} cm^{-1}, $\varepsilon = 1.046 \times 10^9$ M^{-1} cm^{-1}, and $\varepsilon = 0.927 \times 10^9$ M^{-1} cm^{-1} for aspect ratio of 2.51, 2.44, 2.21, and 2.0, respectively, as reported on previous methods.[48,49]

Amino Functionalization of Gold Nanorod (Ends and Sides). AuNR aqueous solutions (0.2–1.0 nM) were prepared from purified stock solution (<72 h of aging), which was adjusted to contain 0.005–0.03 M CTAB concentration. 0.7 mg of AUT (0.58 mM) was added into the solution, and the mixture was homogenized *via* vortexing at 2000 rpm for 1 min and kept at room temperature. To ensure the AuNR stability throughout the reaction, UV–vis spectra was monitored. Typically for preferential end functionalization of AuNR with AUT, 0.03 M CTAB with 30 min of reaction was used. Similarly, for AUT functionalization all around the AuNR surface, reaction was conducted at 0.005 M CTAB for 1 h. However, while using shorter alkylthiol linkers, AuNR was less stable during the reaction under the same condition. For AHT functionalization all around AuNR, the reaction was performed for 1 h at 0.03 M CTAB concentration. Similarly, to achieve APT spacer between AuNR and QD, 0.03 M CTAB was used with 5 min of reaction. The short time and high CTAB concentration were chosen to ensure the stability of AuNRs throughout the reaction.

Thiolation of QD, AuNR, and Dithiol Coupling. A 1 mM solution of Traut's reagent was prepared fresh in pH 9.8 water (NaOH). Amine functionalized QD (10 μM, stock aqueous solution) was added into the solution in order to achieve 1:1 to 1:12.5 ratio of AuNR:QD (typically 0.2–2.5 nM QD concentration) into the final solution. The solution was vortexed for 1 min and kept at room temperature for 15 min. Immediately after that, the solution of amino functionalized AuNRs was added into the reaction and vortexed for another 2 min. To ensure the QD attachment only at the ends of AuNR 0.2 nM of AUT end functionalized AuNR (0.03 M CTAB with 30 min of reaction) was used with 0.2 nM of Traut functionalized QD. Similarly to ensure QD all-around of AuNR, AUT functionalized all-around AuNR (0.005 M CTAB for 1 h) was used with higher QD (Traut functionalized) concentration.

Silica Encapsulation. Silica coating was done by a modified Stober technique following a protocol established for AuNR encapsulation.[66,49] Typically, 4.2 mM concentration of MPTES was prepared in 1 mL ethanol. On a freshly prepared QD_n/AuNR (2 mL), 50 μL of 0.1 NaOH was added to adjust the solution to pH 10. Immediately, under rigorous vortexing, the MPTES in ethanol was added dropwise and stirred for 36 h at room temperature. After the reaction, the product was purified by centrifugation for 15 min at 15 000 rpm, and the residue was dissolved in ethanol. The samples were drop dried on TEM grid for, imaging and UV–vis was monitored in ethanol/water mixture.

Characterization. *Optical Characterization.* UV–vis–NIR spectra were acquired with a Cary 5000 UV–vis–NIR spectrophotometer to monitor the progress of the reaction and the stability of the product in situ. Photoluminescence spectra were recorded using a luminescence spectrometer (JY Horiba, Fluorolog 3) with a cooled CCD detector and a xenon lamp excitation source with excitation from 350 to 550 nm and emission from 600 to 700 nm at an integration time of 0.2 s and an excitation and emission slit width of 2 nm. For PL measurement, control QD solution was prepared by adding equimolar concentration of CTAB and Traut's reagent, similar to that was used in the assembly of QD_n/AuNR. Dark field scattering images were captured with an upright fluorescence microscope (BX41, Olympus) equipped with a commercially available dark-field condenser (N.A. 0.7–1.3, CytoViva, Inc., USA). A hollow cone of light (halogen lamp) was focused by the dark-field condenser, and only the light scattered by AuNR could be collected by a 100× oil immersion objective. Therefore, under the dark-field mode, the background is black and the AuNR appears as bright spots. When the halogen lamp is off and the mercury lamp is on with green 610 long-pass filters (with fwhm 25 nm) in place, the imaging mode is switched to the fluorescence mode (excitation at 570 nm, emission at 610 nm). An CCD coupled on the top of the microscope was used to record the scattering and fluorescence images independently. Data were processed using Image J software (National Institutes of Health, Bethesda, MD).

Electron Microscopy. Morphology and mean size of nanoparticles were determined by Philips CM200 LaB6 TEM at 200 kV. Electron tomography was performed on a C_s-corrected FEI Titan transmission electron microscope operating at 300 kV in scanning transmission electron microscopy (STEM) mode with spot size 6, gun lens 1, and a convergence angle of 9.6 mrad. To form the images, scattered electrons were collected using a Fischione high angle annular dark field (HAADF) detector at a camera length of 105 mm, with an inner detector angle of 60 mrad and an outer detector angle of 300 mrad. The annular detector is placed at a high enough angle such that the contribution from Rutherford scattering is maximized and diffraction contrast is minimized while adequate signal is maintained. Tilt series were collected over a range of −65 to +65 degrees, with a 2 degree tilt increment. Cross correlation alignment was performed to subpixel accuracy after acquisition. Model Based Iterative Reconstruction (MBIR, www.OpenMBIR.org) was used for reconstruction of the aligned data.[62] X-ray energy dispersive spectroscopy (XEDS) was done in STEM mode with a sample tilt of 15 degrees and an EDAX detector. Elemental maps based on intensity of the various XEDS lines were generated using the FEI TIA software package. K, L, and M refer to the core electron band from which an electron was ejected because of the incident electron, and the subscripts α and β indicate which band the electron filling the hole came from (1 band above for α, and 2 bands above for β).

Conflict of Interest: The authors declare no competing financial interest.

Acknowledgment. The authors would like to acknowledge Dr. Peter A. Mirau and Dr. Hilmar Koerner for very valuable comments in the manuscript and Dr. Hilmar Koerner for his assistance with the graphics in Figure 1. This work was completed at Air Force Research Laboratory (AFRL) at Wright Patterson Air Force Base with funding from Materials and Manufacturing Directorate, as well as Air Force Office of Scientific Research.

Supporting Information Available: Experimental details including discussion of the functionalization and assembly, as well as additional UV−vis−NIR spectra, dynamic light scattering, transmission electron microscopy images and video of 3-dimensional tomography reconstruction of silica coated QD_n/AuNR architecture. This material is available free of charge *via* the Internet at http://pubs.acs.org.

REFERENCES AND NOTES

1. Stockman, M. I. Criterion for Negative Refraction with Low Optical Losses from a Fundamental Principle of Causality. *Phys. Rev. Lett.* **2007**, *98*, 177404.
2. Stockman, M. I. Spaser Action, Loss Compensation, and Stability in Plasmonic Systems with Gain. *Phys. Rev. Lett.* **2011**, *106*, 156802.
3. Polman, A.; Atwater, H. A. Photonic Design Principles for Ultrahigh-Efficiency Photovoltaics. *Nat. Mater.* **2012**, *11*, 174–177.
4. Lakowicz, J. R.; Ray, K.; Chowdhury, M.; Szmacinski, H.; Fu, Y.; Zhang, J.; Nowaczyk, K. Plasmon-Controlled Fluorescence: A New Paradigm in Fluorescence Spectroscopy. *Analyst* **2008**, *133*, 1308–1346.
5. Yuan, Z.; Kardynal, B. E.; Stevenson, R. M.; Shields, A. J.; Lobo, C. J.; Cooper, K.; Beattie, N. S.; Ritchie, D. A.; Pepper, M. Electrically Driven Single-Photon Source. *Science* **2002**, *295*, 102–105.
6. Curto, A. G.; Volpe, G.; Taminiau, T. H.; Kreuzer, M. P.; Quidant, R.; van Hulst, N. F. Unidirectional Emission of a Quantum Dot Coupled to a Nanoantenna. *Science* **2010**, *329*, 930–933.
7. Yin, Y.; Alivisatos, A. P. Colloidal Nanocrystal Synthesis and the Organic-Inorganic Interface. *Nature* **2005**, *437*, 664–670.
8. Smith, A. M.; Nie, S. Semiconductor Nanocrystals: Structure, Properties, and Band Gap Engineering. *Acc. Chem. Res.* **2009**, *43*, 190–200.
9. Nirmal, M.; Brus, L. Luminescence Photophysics in Semiconductor Nanocrystals. *Acc. Chem. Res.* **1998**, *32*, 407–414.
10. Achermann, M. Exciton−Plasmon Interactions in Metal−Semiconductor Nanostructures. *J. Phys. Chem. Lett.* **2010**, *1*, 2837–2843.
11. Gu, Y.; Wang, L.; Ren, P.; Zhang, J.; Zhang, T.; Martin, O. J. F.; Gong, Q. Surface-Plasmon-Induced Modification on the Spontaneous Emission Spectrum *via* Subwavelength-Confined Anisotropic Purcell Factor. *Nano Lett.* **2012**, *12*, 2488–2493.
12. Gómez, D. E.; Vernon, K. C.; Mulvaney, P.; Davis, T. J. Surface Plasmon Mediated Strong Exciton−Photon Coupling in Semiconductor Nanocrystals. *Nano Lett.* **2010**, *10*, 274–278.
13. Gérard, J. M.; Sermage, B.; Gayral, B.; Legrand, B.; Costard, E.; Thierry-Mieg, V. Enhanced Spontaneous Emission by Quantum Boxes in a Monolithic Optical Microcavity. *Phys. Rev. Lett.* **1998**, *81*, 1110–1113.
14. Khanal, B. P.; Pandey, A.; Li, L.; Lin, Q.; Bae, W. K.; Luo, H.; Klimov, V. I.; Pietryga, J. M. Generalized Synthesis of Hybrid Metal−Semiconductor Nanostructures Tunable from the Visible to the Infrared. *ACS Nano* **2012**, *6*, 3832–3840.
15. Nikoobakht, B.; Burda, C.; Braun, M.; Hun, M.; El-Sayed, M. A. The Quenching of Cdse Quantum Dots Photoluminescence by Gold Nanoparticles in Solution. *Photochem. Photobiol.* **2002**, *75*, 591–597.
16. Zhao, L.; Ming, T.; Chen, H.; Liang, Y.; Wang, J. Plasmon-Induced Modulation of the Emission Spectra of the Fluorescent Molecules near Gold Nanorods. *Nanoscale* **2011**, *3*, 3849–3859.
17. Li, X.; Qian, J.; Jiang, L.; He, S. Fluorescence Quenching of Quantum Dots by Gold Nanorods and Its Application to DNA Detection. *Appl. Phys. Lett.* **2009**, *94*, 063111.
18. Su, H.; Zhong, Y.; Ming, T.; Wang, J.; Wong, K. S. Extraordinary Surface Plasmon Coupled Emission Using Core/Shell Gold Nanorods. *J. Phys. Chem. C* **2012**, *116*, 9259–9264.
19. Cohen-Hoshen, E.; Bryant, G. W.; Pinkas, I.; Sperling, J.; Bar-Joseph, I. Exciton−Plasmon Interactions in Quantum Dot−Gold Nanoparticle Structures. *Nano Lett.* **2012**, *12*, 4260–4264.
20. Gueroui, Z.; Libchaber, A. Single-Molecule Measurements of Gold-Quenched Quantum Dots. *Phys. Rev. Lett.* **2004**, *93*, 166108.
21. Peng, B.; Zhang, Q.; Liu, X.; Ji, Y.; Demir, H. V.; Huan, C. H. A.; Sum, T. C.; Xiong, Q. Fluorophore-Doped Core−Multishell Spherical Plasmonic Nanocavities: Resonant Energy Transfer toward a Loss Compensation. *ACS Nano* **2012**, *6*, 6250–6259.
22. Kulakovich, O.; Strekal, N.; Yaroshevich, A.; Maskevich, S.; Gaponenko, S.; Nabiev, I.; Woggon, U.; Artemyev, M. Enhanced Luminescence of Cdse Quantum Dots on Gold Colloids. *Nano Lett.* **2002**, *2*, 1449–1452.
23. Anger, P.; Bharadwaj, P.; Novotny, L. Enhancement and Quenching of Single-Molecule Fluorescence. *Phys. Rev. Lett.* **2006**, *96*, 113002.
24. Pons, T.; Medintz, I. L.; Sapsford, K. E.; Higashiya, S.; Grimes, A. F.; English, D. S.; Mattoussi, H. On the Quenching of Semiconductor Quantum Dot Photoluminescence by Proximal Gold Nanoparticles. *Nano Lett.* **2007**, *7*, 3157–3164.
25. De Luca, A.; Grzelczak, M. P.; Pastoriza-Santos, I.; Liz-Marzan, L. M.; La Deda, M.; Striccoli, M.; Strangi, G. Dispersed and Encapsulated Gain Medium in Plasmonic Nanoparticles: A Multipronged Approach to Mitigate Optical Losses. *ACS Nano* **2011**, *5*, 5823–5829.
26. Todorov, Y.; Sagnes, I.; Abram, I.; Minot, C. Purcell Enhancement of Spontaneous Emission from Quantum Cascades inside Mirror-Grating Metal Cavities at THz Frequencies. *Phys. Rev. Lett.* **2007**, *99*, 223603.
27. Lodahl, P.; Floris van Driel, A.; Nikolaev, I. S.; Irman, A.; Overgaag, K.; Vanmaekelbergh, D.; Vos, W. L. Controlling the Dynamics of Spontaneous Emission from Quantum Dots by Photonic Crystals. *Nature* **2004**, *430*, 654–657.
28. Ming, T.; Chen, H.; Jiang, R.; Li, Q.; Wang, J. Plasmon-Controlled Fluorescence: Beyond the Intensity Enhancement. *J. Phys. Chem. Lett.* **2011**, *3*, 191–202.

29. Le Ru, E. C.; Etchegoin, P. G.; Grand, J.; Félidj, N.; Aubard, J.; Lévi, G. Mechanisms of Spectral Profile Modification in Surface-Enhanced Fluorescence. *J. Phys. Chem. C* **2007**, *111*, 16076–16079.
30. Kinkhabwala, A.; Yu, Z.; Fan, S.; Avlasevich, Y.; Mullen, K.; Moerner, W. E. Large Single-Molecule Fluorescence Enhancements Produced by a Bowtie Nanoantenna. *Nat. Photonics* **2009**, *3*, 654–657.
31. Zhang, J.; Fu, Y.; Chowdhury, M. H.; Lakowicz, J. R. Enhanced Förster Resonance Energy Transfer on Single Metal Particle. 2. Dependence on Donor−Acceptor Separation Distance, Particle Size, and Distance from Metal Surface. *J. Phys. Chem. C* **2007**, *111*, 11784–11792.
32. Drexhage, K. H. Influence of a Dielectric Interface on Fluorescence Decay Time. *J. Lumin.* **1970**, *1*−*2*, 693–701.
33. Dirac, P. A. M. The Quantum Theory of the Emission and Absorption of Radiation. *Proc. R. Soc. London, Ser. A* **1927**, *114*, 243–265.
34. Barnes, W. L. Fluorescence near Interfaces: The Role of Photonic Mode Density. *J. Mod. Opt.* **1998**, *45*, 661–699.
35. Duan, J.; Nepal, D.; Park, K.; Haley, J. E.; Vella, J. H.; Urbas, A. M.; Vaia, R. A.; Pachter, R. Computational Prediction of Molecular Photoresponse Upon Proximity to Gold Nanorods. *J. Phys. Chem. C* **2011**, *115*, 13961–13967.
36. Lu, G.; Zhang, T.; Li, W.; Hou, L.; Liu, J.; Gong, Q. Single-Molecule Spontaneous Emission in the Vicinity of an Individual Gold Nanorod. *J. Phys. Chem. C* **2011**, *115*, 15822–15828.
37. Fu, Y.; Zhang, J.; Lakowicz, J. R. Plasmon-Enhanced Fluorescence from Single Fluorophores End-Linked to Gold Nanorods. *J. Am. Chem. Soc.* **2010**, *132*, 5540–5541.
38. Ma, X.; Fletcher, K.; Kipp, T.; Grzelczak, M. P.; Wang, Z.; Guerrero-Martínez, A.; Pastoriza-Santos, I.; Kornowski, A.; Liz-Marzán, L. M.; Mews, A. Photoluminescence of Individual Au/CdSe Nanocrystal Complexes with Variable Interparticle Distances. *J. Phys. Chem. Lett.* **2011**, *2*, 2466–2471.
39. Bardhan, R.; Grady, N. K.; Cole, J. R.; Joshi, A.; Halas, N. J. Fluorescence Enhancement by Au Nanostructures: Nanoshells and Nanorods. *ACS Nano* **2009**, *3*, 744–752.
40. Li, X.; Kao, F.-J.; Chuang, C.-C.; He, S. Enhancing Fluorescence of Quantum Dots by Silica-Coated Gold Nanorods under One- and Two-Photon Excitation. *Opt. Express* **2010**, *18*, 11335–11346.
41. Pompa, P. P.; Martiradonna, L.; Torre, A. D.; Sala, F. D.; Manna, L.; De Vittorio, M.; Calabi, F.; Cingolani, R.; Rinaldi, R. Metal-Enhanced Fluorescence of Colloidal Nanocrystals with Nanoscale Control. *Nat. Nanotechnol.* **2006**, *1*, 126–130.
42. Viste, P.; Plain, J.; Jaffiol, R.; Vial, A.; Adam, P. M.; Royer, P. Enhancement and Quenching Regimes in Metal−Semiconductor Hybrid Optical Nanosources. *ACS Nano* **2010**, *4*, 759–764.
43. Reineck, P.; Gómez, D.; Ng, S. H.; Karg, M.; Bell, T.; Mulvaney, P.; Bach, U. Distance and Wavelength Dependent Quenching of Molecular Fluorescence by Au@SiO$_2$ Core−Shell Nanoparticles. *ACS Nano* **2013**, *7*, 6636–6648.
44. Liaw, J.-W.; Tsai, H.-Y.; Huang, C.-H. Size-Dependent Surface Enhanced Fluorescence of Gold Nanorod: Enhancement or Quenching. *Plasmonics* **2012**, *7*, 543–553.
45. Jun, Y. C.; Pala, R.; Brongersma, M. L. Strong Modification of Quantum Dot Spontaneous Emission *via* Gap Plasmon Coupling in Metal Nanoslits. *J. Phys. Chem. C* **2009**, *114*, 7269–7273.
46. Wang, T.; Zhuang, J.; Lynch, J.; Chen, O.; Wang, Z.; Wang, X.; LaMontagne, D.; Wu, H.; Wang, Z.; Cao, Y. C. Self-Assembled Colloidal Superparticles from Nanorods. *Science* **2012**, *338*, 358–363.
47. Kuzyk, A.; Schreiber, R.; Fan, Z.; Pardatscher, G.; Roller, E.-M.; Hogele, A.; Simmel, F. C.; Govorov, A. O.; Liedl, T. DNA-Based Self-Assembly of Chiral Plasmonic Nanostructures with Tailored Optical Response. *Nature* **2012**, *483*, 311–314.
48. Park, K.; Koerner, H.; Vaia, R. A. Depletion-Induced Shape and Size Selection of Gold Nanoparticles. *Nano Lett.* **2010**, *10*, 1433–1439.
49. Nepal, D.; Park, K.; Vaia, R. A. High-Yield Assembly of Soluble and Stable Gold Nanorod Pairs for High-Temperature Plasmonics. *Small* **2012**, *8*, 1013–1020.
50. Nikoobakht, B.; El-Sayed, M. A. Preparation and Growth Mechanism of Gold Nanorods Using Seed-Mediated Growth Method. *Chem. Mater.* **2003**, *15*, 1957–1962.
51. Ye, X.; Jin, L.; Caglayan, H.; Chen, J.; Xing, G.; Zheng, C.; Doan-Nguyen, V.; Kang, Y.; Engheta, N.; Kagan, C. R.; *et al.* Improved Size-Tunable Synthesis of Monodisperse Gold Nanorods through the Use of Aromatic Additives. *ACS Nano* **2012**, *6*, 2804–2817.
52. Park, K.; Drummy, L. F.; Wadams, R. C.; Koerner, H.; Nepal, D.; Fabris, L.; Vaia, R. A. Growth Mechanism of Gold Nanorods. *Chem. Mater.* **2013**, *25*, 555–563.
53. Woehrle, G. H.; Brown, L. O.; Hutchison, J. E. Thiol-Functionalized, 1.5-Nm Gold Nanoparticles through Ligand Exchange Reactions: Scope and Mechanism of Ligand Exchange. *J. Am. Chem. Soc.* **2005**, *127*, 2172–2183.
54. Chen, F.; Li, X.; Hihath, J.; Huang, Z.; Tao, N. Effect of Anchoring Groups on Single-Molecule Conductance: Comparative Study of Thiol-, Amine-, and Carboxylic-Acid-Terminated Molecules. *J. Am. Chem. Soc.* **2006**, *128*, 15874–15881.
55. Storhoff, J. J.; Mirkin, C. A. Programmed Materials Synthesis with DNA. *Chem. Rev.* **1999**, *99*, 1849–1862.
56. Jennings, T. L.; Becker-Catania, S. G.; Triulzi, R. C.; Tao, G.; Scott, B.; Sapsford, K. E.; Spindel, S.; Oh, E.; Jain, V.; Delehanty, J. B.; *et al.* Reactive Semiconductor Nanocrystals for Chemoselective Biolabeling and Multiplexed Analysis. *ACS Nano* **2011**, *5*, 5579–5593.
57. Guerrero-Martínez, A.; Pérez-Juste, J.; Liz-Marzán, L. M. Recent Progress on Silica Coating of Nanoparticles and Related Nanomaterials. *Adv. Mater.* **2010**, *22*, 1182–1195.
58. Jokerst, J. V.; Thangaraj, M.; Kempen, P. J.; Sinclair, R.; Gambhir, S. S. Photoacoustic Imaging of Mesenchymal Stem Cells in Living Mice *via* Silica-Coated Gold Nanorods. *ACS Nano* **2012**, *6*, 5920–5930.
59. Chanana, M.; Liz-Marzán, L. M. Coating Matters: The Influence of Coating Materials on the Optical Properties of Gold Nanoparticles. *Nanophotonics* **2012**, *1*, 199–220.
60. Carion, O.; Mahler, B.; Pons, T.; Dubertret, B. Synthesis, Encapsulation, Purification and Coupling of Single Quantum Dots in Phospholipid Micelles for Their Use in Cellular and *in Vivo* Imaging. *Nat. Protoc.* **2007**, *2*, 2383–2390.
61. Leary, R.; Midgley, P. A.; Thomas, J. M. Recent Advances in the Application of Electron Tomography to Materials Chemistry. *Acc. Chem. Res.* **2012**, *45*, 1782–1791.
62. Venkatakrishnan, S.; Drummy, L.; Jackson, M.; De Graef, M.; Simmons, J.; Bouman, C. Bayesian Tomographic Reconstruction for High Angle Annular Dark Field (HAADF) Scanning Transmission Electron Microscopy (STEM). In *2012 IEEE Statistical Signal Processing Workshop (SSP)*, IEEE, Ann Arbor, MI, 5−8 August 2012, pp. 680−683.
63. Nann, T.; Mulvaney, P. Single Quantum Dots in Spherical Silica Particles. *Angew. Chem., Int. Ed.* **2004**, *43*, 5393–5396.
64. Duan, J.; Park, K.; MacCuspie, R. I.; Vaia, R. A.; Pachter, R. Optical Properties of Rodlike Metallic Nanostructures: Insight from Theory and Experiment. *J. Phys. Chem. C* **2009**, *113*, 15524–15532.
65. Park, K.; Vaia, R. A. Synthesis of Complex Au/Ag Nanorods by Controlled Overgrowth. *Adv. Mater.* **2008**, *20*, 3882–3886.
66. Gorelikov, I.; Matsuura, N. Single-Step Coating of Mesoporous Silica on Cetyltrimethyl Ammonium Bromide-Capped Nanoparticles. *Nano Lett.* **2008**, *8*, 369–373.